Earth, Planets and Space

FULL PAPER Open Access

Utilization of a meteorological satellite as a space telescope: the lunar mid-infrared spectrum as seen by Himawari-8

Gaku Nishiyama[1*], Noriyuki Namiki[2,3], Seiji Sugita[1] and Shinsuke Uno[4]

Abstract

The Japanese meteorological satellite Himawari-8 has captured the Earth's atmosphere and stars, planets, and the Moon in its field of view, enabling us to capture their spectroscopy with 16 bands from visible to mid-infrared wavelengths. The nine infrared bands in the Advanced Himawari Imager (AHI) onboard Himawari-8 are unique in space-borne observations and are potentially useful for lunar science. In addition, infrared bands of AHI cover wavelengths similar to those of other interplanetary instruments and thus are useful for calibrations. However, infrared AHI data have not yet been investigated in planetary science. To confirm the utility of AHI for planetary science, we develop a procedure to retrieve the lunar infrared spectrum and compare it with thermal conduction simulations. Our analysis shows that lunar brightness temperature curves can be obtained in the morning, evening, and nighttime for all nine bands. Particularly at 8.5 μm, they show a good agreement with previous observations by the Diviner radiometer onboard NASA's Lunar Reconnaissance Orbiter. As pointed out previously, the brightness temperatures differ between the bands, indicating temperature mixing within a pixel. Our simulation suggests that surface roughness as steep as those measured at the Apollo landing sites significantly contributes to the observed brightness temperature differences in the morning and evening; however, nighttime brightness temperatures are greatly affected by rocks with higher thermal inertia than the regolith. The rock abundances are estimated to be 0.18–0.48% and 6.1–10.3% at the equator and within Tycho crater, respectively. Our estimations from AHI data are consistent with those of Diviner. These results support the idea that AHI potentially serves as a space telescope for future lunar and planetary sciences, for example, for constraining water content on the lunar surface.

Keywords: Meteorological satellite, Moon, Infrared spectrum, Regolith, Space telescope, Himawari-8, Lunar surface roughness, Diviner, Rock abundance, Anisothermality

*Correspondence: gaku.nishiyama@eps.s.u-tokyo.ac.jp

[1] Department of Earth and Planetary Science, Graduate School of Science, University of Tokyo, Tokyo 113-0033, Japan
Full list of author information is available at the end of the article

Graphical Abstract

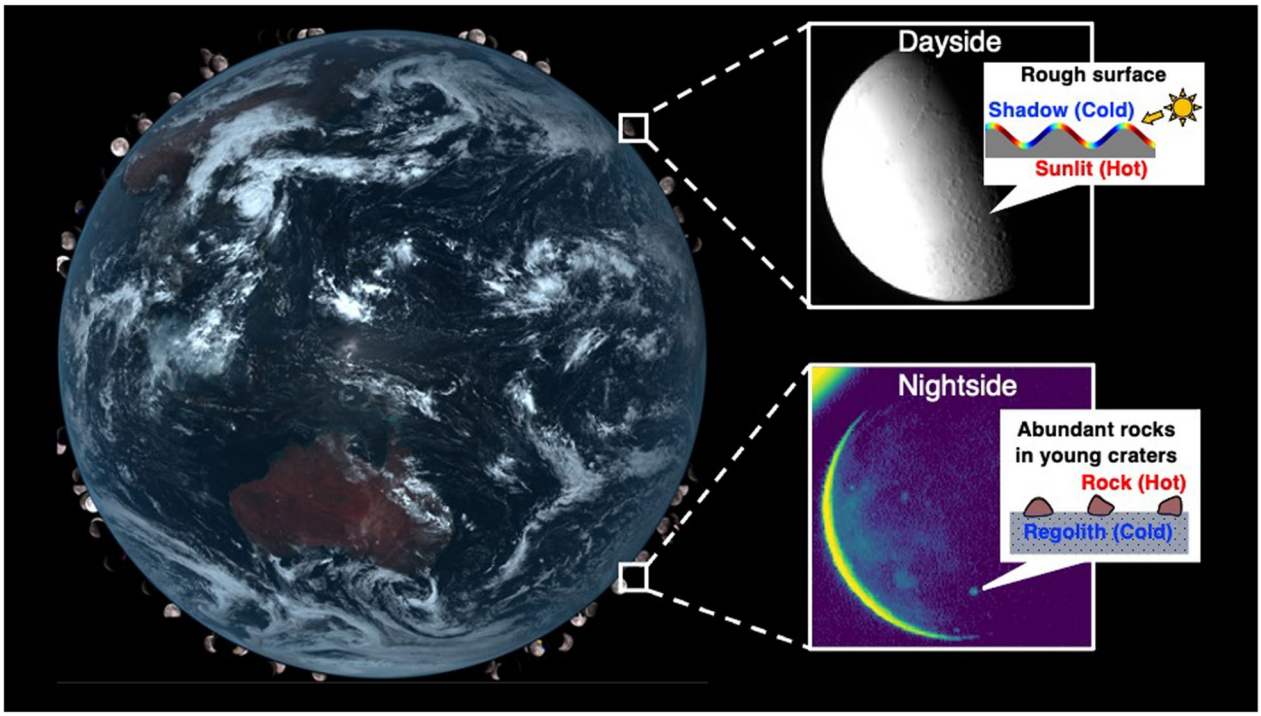

Introduction

Since the beginning of its operation in 2015, the Japanese meteorological satellite Himawari-8 has captured images of the Earth with high resolution in both time and space. Every 10 min, the Advanced Himawari Imager (AHI) onboard Himawari-8 scans a full-disk imagery of the Earth. Additionally, the observation capability of AHI has improved from its predecessor, with a spatial resolution of 2 km or higher on the terrestrial equator (Bessho et al. 2016; Okuyama et al. 2018). During each 10-min scanning cycle, AHI also covers the space surrounding the Earth for calibration; namely, stars, planets, and the Moon are captured simultaneously in the field of view of AHI. The high performance of AHI sometimes enables us to resolve some of these unexpected targets spatially. Such images of celestial bodies have only recently been used in astronomical and planetary research. For example, Taniguchi et al. (2022) obtained high-cadence light curves of the red supergiant star Betelgeuse using AHI and examined its temporal dimming event between late 2019 and early 2020.

Another significant characteristic of AHI is its plentiful bands ranging from visible to mid-infrared wavelengths (Table 1). AHI has three visible (0.4–0.7 μm), four near-infrared (0.8–4 μm), and nine mid-infrared (6–14 μm) bands (Okuyama et al. 2018). The mid-infrared bands are highly notable in lunar science because few spaceborne remote sensing studies of the Moon have been conducted at these wavelengths. Figure 1 shows the response functions of bands 8–16 of AHI compared with those of other instruments used in planetary explorations. For example, the most sophisticated lunar observation has been conducted by the Diviner Radiometer onboard the Lunar Reconnaissance Orbiter (LRO) with four bands over 7.5–23 μm (Paige et al. 2010). However, three of these are gathered at approximately 8 μm to identify the lunar mineralogy (Greenhagen et al. 2010). It should also be noted that lunar observations using ground-based instruments are affected by the Earth's atmospheric window at mid-infrared wavelengths, particularly below 8 μm. To avoid this uncertainty, Honniball et al. (2021) used the NASA/DLR Stratospheric Observatory for Infrared Astronomy (SOFIA) telescope flown on an aircraft, but only Clavius crater and its surroundings were observed. Thus, the mid-infrared images taken by AHI are unique and potentially compensate for other lunar and planetary datasets.

The mid-infrared spectrum of airless bodies such as the Moon is important for understanding their surface physical properties. Previous multiband infrared observations have observed differences in brightness temperatures

Table 1 Summary of the AHI instrumental properties of every band (Griffith 2015; Takahashi and Okuyama 2017)

Band	Central wavelength (μm)	Bandwidth (μm)	Accuracy	Instantaneous field-of-view (μrad)		Detector type	Number of detectors
				NS	EW		
1	0.4703	0.0407	585@100% albedo	22.9	22.9	Si	676
2	0.5105	0.0308	645@100% albedo				
3	0.6399	0.0817	459@100% albedo	10.5	12.4		1460
4	0.8563	0.0345	420@100% albedo	22.9	22.9	HgCdTe	676
5	1.6098	0.0409	912@100% albedo	42.0	51.5		372
6	2.2570	0.0441	688@100% albedo				
7	3.8848	0.2006	0.21@300K	47.7	51.5		332
8	6.2383	0.8219	0.13@240K				
9	6.9395	0.4019	0.039@300K				
10	7.3471	0.1871	0.13@240K				
11	8.5905	0.3727	0.042@300K				
12	9.6347	0.3779	0.052@300K				
13	10.4029	0.4189	0.077@300K	38.1	34.3		408
14	11.2432	0.6678	0.063@300K				
15	12.3828	0.9656	0.087@300K				
16	13.2844	0.5638	0.22@300K				

The accuracy values in bands 1–6 and 7–16 are the signal-to-noise ratio and noise-equivalent temperature, respectively. The instantaneous field-of-view of each detector differs between the north–south (NS) and east–west (EW) directions on the Moon

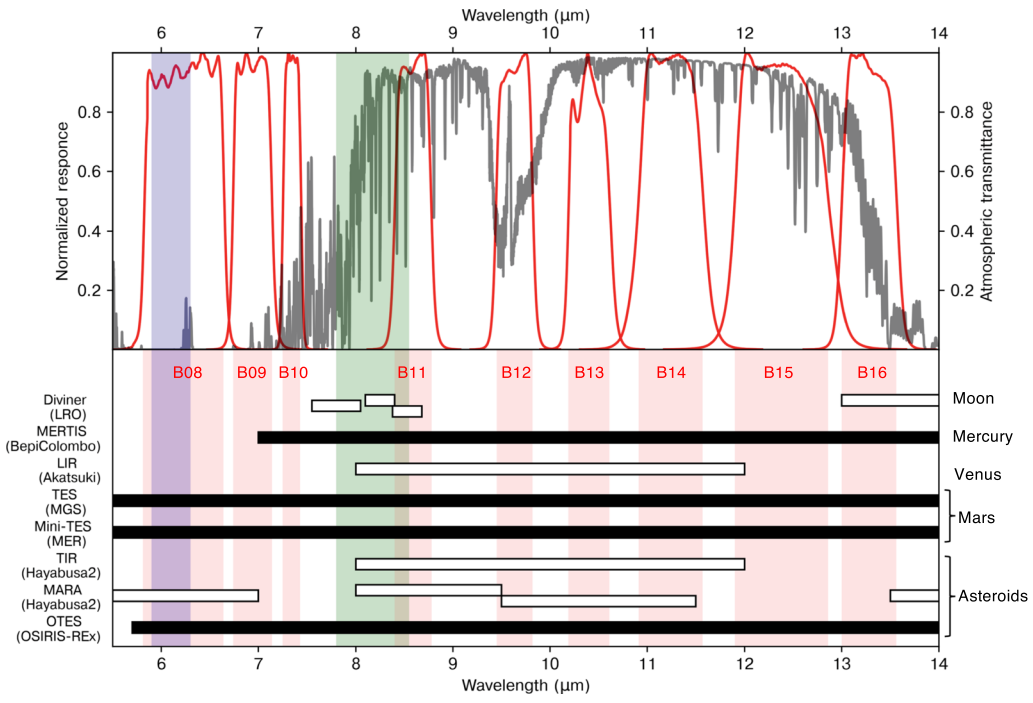

Fig. 1 (Upper) The AHI's nine spectral passbands in mid-infrared wavelength. The red lines are the normalized response functions of bands 8–16 of AHI. The gray line is the atmospheric transmission calculated by ATRAN (Lord (1992); https://atran.arc.nasa.gov/cgi-bin/atran/atran.cgi). The blue and green shades correspond to wavelengths of water emission and Christiansen feature, respectively. (Lower) Comparison with other instruments onboard planetary exploration missions. The white and black bars are the response ranges of imagers and spectrometers on interplanetary spacecraft. The red shades and numbers are the AHI coverages and corresponding band names

among wavelengths, the so-called anisothermality. Anisothermality reflects the temperature distribution owing to the surficial characteristics within the field of view. Therefore, in addition to its temporal variation, the infrared spectrum is useful for estimating the thermal inertia (Hayne et al. 2017; Howett et al. 2010; Shimaki et al. 2020), millimeter-scale roughness (Bandfield et al. 2015; Davidsson et al. 2015; Hapke, 1984), and rock abundance (Bandfield et al. 2011; Nowicki and Christensen, 2007). These physical properties are critical for estimating the thermal environment and evaluating the safety of landing missions (e.g., Wu et al. 2018) and stability of volatiles such as water (Davidsson and Hosseini 2021).

Moreover, the infrared spectrum contains various types of compositional information. The SOFIA observation recently detected a spectral signature of molecular water at 6 μm (Honniball et al. 2021). This signature is within the coverage of band 8 of AHI. Unlike the 3-μm hydration feature observed by the Chandrayaan-1 and Deep Impact spacecraft (Pieters et al. 2009; Sunshine et al. 2009), water molecules are discriminable from hydroxyl compounds at the 6-μm emission. The presence of water is necessary for future space development; thus, the constraint on water content with the 6-μm spectrum is essential information for lunar explorations hereafter. In addition, the emissivity of the Moon and Mercury has a peak called the Christiansen feature around 8 μm near band 11 of AHI (Salisbury et al. 1970; Sprague et al. 1994). The wavelength of its position is strongly sensitive to plagioclase content (Conel 1969; Nash and Salisbury 1991), enabling the mapping of silicate mineralogy (Greenhagen et al. 2010; Lucey et al. 2021).

In addition to its scientific merits, the infrared data measured from space by AHI are potentially useful for calibrating other planetary explorations. As shown in Fig. 1, the wavelength coverages of infrared imagers and spectrometers employed by interplanetary missions overlap with those of AHI. For instance, the thermal infrared imager (TIR) onboard Hayabusa2 and the longwave infrared camera (LIR) onboard Akatsuki are single-band imagers covering 8–12 μm (Fukuhara et al. 2011; Okada et al. 2017). The MASCOT lander in the Hayabusa2 mission has a radiometer MARA equipped with four multispectral bands over 5–15.5 μm (Grott et al. 2017). The OSIRIS-REx Thermal Emission Spectrometer (OTES) covers a spectral range of 5.7–100 μm (Christensen et al. 2018). In addition, Martian hyperspectral data in the mid-infrared wavelengths have been obtained by the Thermal Emission Spectrometer (TES) on Mars Global Surveyor (Christensen et al. 2001) and the Miniature Thermal Emission Spectrometer (Mini-TES) on Mars Exploration Rovers (Christensen et al. 2003). In the case of an ongoing mission, the BepiColombo spacecraft has a Mercury Radiometer and Thermal Infrared Spectrometer (MERTIS) that covers 7–14 μm (Hiesinger et al. 2020). The sensitivity of some of these infrared radiometers is tested during the cruise to the target body, and the Moon has often been used as an in-flight calibrator.

The lunar images taken by AHI are more useful for calibration than those obtained by previous meteorological satellite instruments. In general, the spatial resolution of the calibrator is preferred to be equal to or better than that of the target instruments, enabling the comparison of the target image without losing any information. The Moon has been resolved better in the AHI observations than in some interplanetary infrared instrument observations. For example, the spatial resolution of the Moon taken by AHI is higher than that taken by TIR before and after the Earth swing-by by an order of magnitude (Okada et al. 2018). In contrast, previous benchmarks using weather satellites cannot resolve lunar images. Müller et al. (2021) utilized the High-Resolution Infrared Radiation Sounder (HIRS) instrument on NOAA and MetOp satellites as benchmarks for their thermal models. Because HIRS cannot resolve lunar radiance spatially, they used only disk-integrated lunar radiance to test their thermophysical and radiometric models. Although their demonstration showed the availability of the single-pixel Moon, benchmarks at every local time were not conducted.

Despite the potential of AHI, its data have not yet been examined in planetary science. Although lunar images in the visible and near-infrared wavelengths have been analyzed to evaluate the modulation transfer function of AHI (Keller et al. 2017), the infrared spectrum of the Moon has not been utilized. This study first develops a procedure to retrieve the lunar infrared spectrum measured from the AHI data. Next, we confirm the utility of AHI by comparing its measurement with the Diviner data on the Moon. We then conduct thermal simulations to constrain the surface roughness and rock abundances from the AHI data and compare them with previous observations to discuss the utility of AHI for lunar science. Finally, we discuss the further utilization of AHI for future planetary science.

AHI data analysis

Preprocessing

To analyze lunar infrared spectroscopy, we used Himawari Standard Data (HSD) published by the Japan Meteorological Agency (Japan Meteorological Agency 2017). In HSD files, full-disk imagery consists of 23 scanning swaths along the east–west direction, covering the area approximately within a 9.6° radius from the Earth's center in total. The conversion coefficients from count to radiance are also included in HSD. The coefficients are

well-calibrated at the beginning of each 10-min timeline with a temperature-controlled blackbody equipped inside AHI (Griffith 2015). The noise of infrared radiance is negligibly small for HgCdTe detectors onboard AHI. Takahashi and Okuyama (2017) reported that the noise-equivalent differential temperature was always smaller than 0.22 K at 300 K in prelaunch ground testing. The characteristics of AHI (Griffith 2015; Takahashi and Okuyama 2017) are summarized in Table 1.

From all the HSDs taken by the end of November 2021, we found 955 images that included the Moon adjacent to the Earth. The Moon is sometimes hidden by the Earth (Fig. 2a and c), cut by the boundaries between scanning swaths (Fig. 2b), or squeezed out of the image (Fig. 2d). By defining quality levels from 1 to 5 and evaluating each lunar image by visual inspection, we selected 248 events with a quality level of 3 or higher, when more than half part of the Moon was captured (Fig. 2f).

AHI image pixels must be linked to longitudes and latitudes on the Moon. First, we estimate the approximate lunar position with SPICE. Next, the differences in the radiance between two neighboring pixels are calculated along the x- and y-axes (Fig. 3) to identify the positions with the maximum differences as the rim candidates of the Moon. We then fit the candidates with a circle and exclude false detections. By iteratively conducting this process, we determine the lunar center. Finally, the lunar orientation in each image is calculated using SPICE. Note that pixels nearby the Earth were excluded because they are affected by the atmospheric refraction of the Earth (see Appendix).

The radiance of each pixel is converted into the brightness temperature of the respective bands. In our analysis, the radiance is fitted to a Planck function by incorporating the response function of AHI for each band under the assumption of an emissivity of 0.95. This emissivity value was chosen following previous works (e.g., Bandfield et al. 2015; Hayne et al. 2017), and the validity of this assumption is discussed later. It should be noted that the brightness temperature at local times from 8 to 16 H is saturated. This is because the count range of AHI is optimized for terrestrial observation, while the lunar radiance around noon is much brighter than the Earth's one in the mid-infrared wavelengths.

Background and noise levels

Owing to a dim halo around the Earth and the Moon in the AHI images, the background level of the interplanetary space is usually non-zero (Fig. 3a). The brightness of the halo increases with that of the Earth or the Moon. For instance, the background level is higher around the full Moons than around the new Moons. In contrast, the intensity decreases with increasing distance from the source. This characteristic of the AHI image is similar to the "broad point-spread-function (PSF)", which was present in some previous spacecraft cameras such as the Optical Navigation Camera

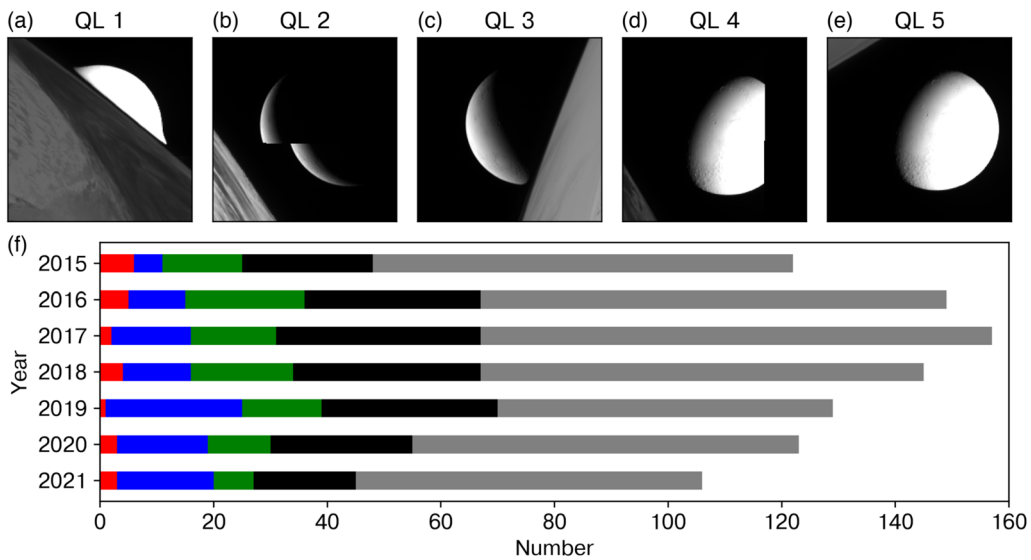

Fig. 2 **a**–**e** Example images of quality level (QL) 1–5. QL of 1, 2, 3, 4, and 5 correspond to the Moon hidden more than half, cut by swath boundaries, hidden partly by the Earth, partly out of the scanned area, and fully captured, respectively. The images were retrieved from the band-13 data taken at 2015/04/01 00:40, 2016/10/26 12:00, 2016/11/23 09:30, 2016/12/09 23:20, and 2017/10/30 23:10. **f** The histogram of the number of QLs for each year from 2015 to 2021. The gray, black, green, blue, and red bars correspond to QL of 1, 2, 3, 4, and 5, respectively

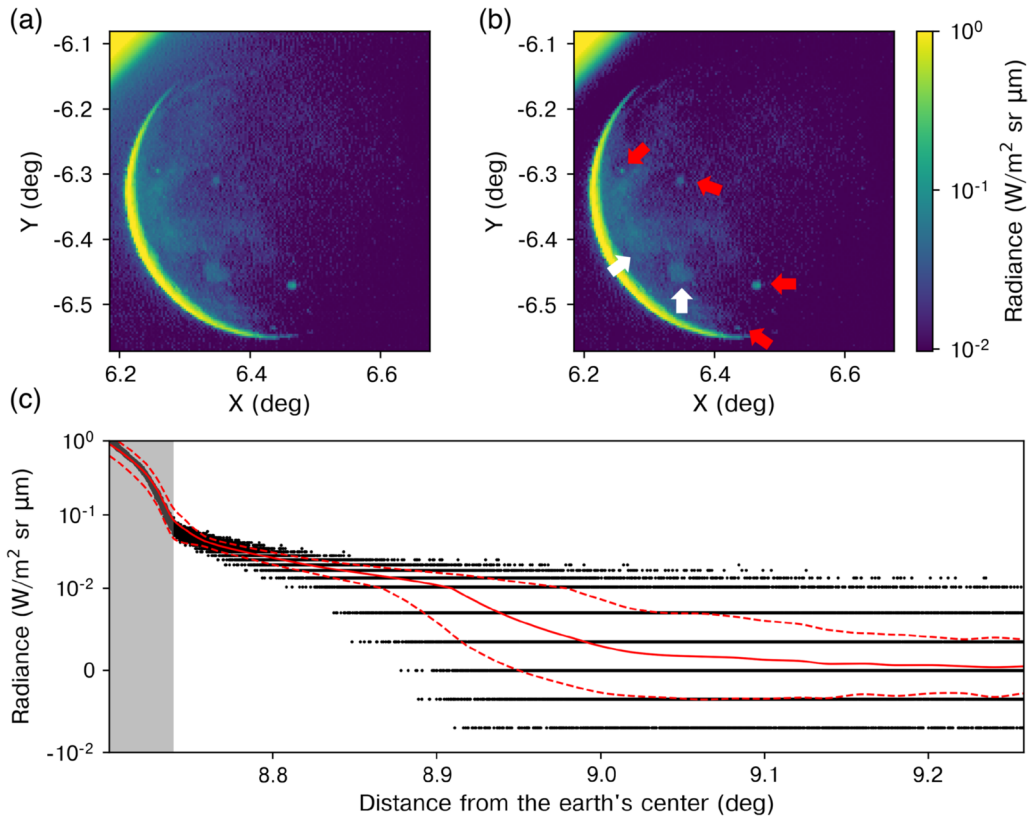

Fig. 3 The lunar images taken at band 14 on 2015/11/09 13:10 **a** before and **b** after the extraction of the broad PSF from the Earth. The red arrows in **b** indicate bright spots corresponding to Aristarchus, Copernicus, Tycho, and Zucchius craters in order from the top. The areas indicated by the left and right white arrows in **b** are Oceanus Procellarum and Mare Humorum, respectively. **c** The broad PSF from the Earth as a function of the distance from the terrestrial center. The black dots are the pixels located outside two lunar radii. The solid and dashed red lines are the average and plus-minus one standard deviation range of the broad PSF, respectively. The left terminator is the rim of the Earth. The gray area is affected by the terrestrial atmosphere

onboard Hayabusa2 and is possibly caused by multiple scattering of light within the optical system (Tatsumi et al. 2019).

We assess the broad PSF in each AHI image and retrieve the background and noise. With the HSD values outside the Earth, we first construct the terrestrial broad-PSF as a polynomial function of the distance from the Earth's center. The average and standard deviation of the radiance in space were used to estimate the background and noise levels of the halo, respectively (Fig. 3c). In this procedure, pixels within two lunar radii from the lunar dayside were excluded because they are contaminated by the lunar broad PSF. After extracting the background halo from HSD, the lunar image becomes clearer (Fig. 3b). Then, the lunar broad PSF is constructed as a function of the distance of the lunar dayside pixels in the same manner as the terrestrial PSF.

Numerical models of lunar surface temperature

Thermophysical model

To interpret the brightness temperatures measured by AHI, we numerically model the surficial temperature and heat transfer of the lunar rock and regolith. Previous works by Davidsson et al. (2015) and Zhang et al. (2019) assumed the radiative equilibrium simply because the thermal diffusion in the ground on the daytime surface is negligible on slowly rotating bodies with low thermal inertia, such as the Moon. According to Bandfield et al. (2015), radiative equilibrium models on the equator predict that the daytime temperatures at local times of 8–16 H match those estimated with heat diffusion models within 1 K. However, unsaturated pixels in HSD are limited to the lunar morning, evening, and night where temperatures are rapidly changing. In addition, the brightness temperatures in HSD indicate the importance of the heat flow between the surface and interior

(described later in the Results section). Therefore, we use the thermal diffusion model instead of the simple radiative equilibrium model.

Our thermophysical model assumes a one-dimensional temperature structure following a heat diffusion equation as follows:

$$\rho c_p \frac{\partial T}{\partial t} = \frac{\partial}{\partial z}\left(K \frac{\partial T}{\partial z}\right) \quad (1)$$

where T is the absolute temperature, t is time, z is the depth from the surface, ρ is the density, c_p is the specific heat, K is the thermal conductivity of the medium. In addition, boundary conditions are critically important in numerical models. At the surface, the sum of the heat transfer and solar flux absorbed by the surface is balanced against the radiative emission energy as follows:

$$K \frac{\partial T}{\partial z}\Big|_{z=0} + (1-A)S\cos\theta_i = \epsilon\sigma T^4 \quad (2)$$

where A is the albedo, S is the solar constant, θ_i is the incident angle, ϵ is the emissivity, and σ is the Stefan–Boltzmann constant. In the simulation, S was constant at 1361 W/m^2 (Kopp and Lean 2011). Using the relationship between the Lunar Orbiter Laser Altimeter (LOLA) data and bond albedos (Hayne et al. 2017), the values of A in mare and highland were assumed to be 0.08 and 0.16, respectively. At the bottom, the heat transfer equals the internal heat flux, that is,

$$K \frac{\partial T}{\partial z}\Big|_{z=z_{bottom}} = Q_{int} \quad (3)$$

where Q_{int} is the heat flux from the lunar interior, and z_{bottom} is the depth of the deepest grid in our simulation. Q_{int} was assumed to be 0.018 W/m^2 as the Apollo measurements (Langseth et al. 1976). z_{bottom} was set to 1 m, where diurnal variations in temperature are negligible.

In our simulations, surficial temperatures are calculated for ten lunar diurnal cycles to sufficiently diminish the effect of the initial conditions. The initial temperature profile in the medium significantly affects the thermal diffusion simulation, but its effect is moderated with time. In our model, the initial temperature was always assumed to be 200 K in the entire layer. Although this initial condition differs from that by Hayne et al. (2017), its effect on our simulation result is negligibly small after ten lunar diurnal cycles. For example, the surface temperature of the regolith at midnight differs by only 2 K between the whole 200-K and Hayne's models.

Anisothermality model

The difference in brightness temperatures among multiple bands helps in understanding the lunar surface properties. In general, if the surface temperatures are uniform in the field of view, the dependence of radiance on the wavelength can be fitted perfectly with a single-temperature Planck function. In contrast, if a pixel contains a wide range of temperatures, a mixture of various non-linear radiances causes brightness temperature differences between bands. This effect is known as anisothermality. Thermal emission from warm surfaces has a larger power at shorter wavelengths than from cold surfaces. In other words, brightness temperatures at shorter wavelengths are more subject to hot surfaces than to cold ones. As a result, brightness temperatures increase with decreasing wavelength, approaching the highest temperature in the field of view. Considering this property, multispectral anisothermality measurements have been used to characterize the surface properties of the Moon and other planets (e.g., Bandfield et al. 2015, 2011).

One cause of anisothermality in airless bodies is surficial roughness. Roughness is important in warming or cooling the surface because slopes change the incident angles and hence the energy flux from the sun. Especially in areas of high incident angles where unsaturated HSD is available, surfaces on rough terrain are sunlit or shadowed, depending on their slope orientation with respect to the sun. This causes widely heterogeneous temperatures within the field of view. In practice, previous in situ measurements and remote sensing with laser altimeters, radiometers, and radar have revealed that the lunar surface has various slopes at millimetric-to-kilometric scales (Helfenstein and Shepard 1999; Kreslavsky et al. 2013; Rosenburg et al. 2011; Shepard et al. 1995). Considering that the HSD resolution is 23 km or larger on the Moon in the infrared bands, the area corresponding to each HSD pixel is probably anisothermal owing to such roughness.

To quantitatively predict anisothermality by roughness, we employ a simple Gaussian roughness model used for previous numerical models of lunar and Martian thermal infrared radiance (Bandfield 2009; Bandfield et al. 2015; Bandfield and Edwards 2008; Davidsson et al. 2015). This is a statistical approach for estimating the temperature distribution on rough terrains without high computational cost. We first define the slope distributions for various root mean square (RMS) slope angles. To consider km-scale relief, a Gaussian slope distribution is set on each DEM facet of the LOLA topography data with the maximum spherical harmonic degree and order of 2050. We then simulate the surface temperatures for each set of slopes and azimuths. Finally, the radiative emission is integrated for the slope distribution, incorporating the statistical fraction of shaded surfaces dependent on the incidence and emission angles (see Appendix).

Anisothermality is also caused by the rock mixture in the regolith. The temperature response of the medium

is determined by its physical properties. For highly insulating regolith fines, the lunar diurnal cycle changes its temperature profile only within a depth of several centimeters. However, the temporal variation in temperature in highly conducting rocks reaches meter-scale depths. This difference in thermal inertia between the rock and regolith causes a large temperature contrast between these materials, resulting in anisothermal surfaces on the Moon.

The temperature difference between the rock and regolith is simulated using a one-dimensional thermal model, using the density structure, specific heat, and thermal conductivity from previous studies. For rock temperatures, the physical properties of lunar materials returned by Apollo 11 and 12 missions were used. Based on lunar vesicular igneous sample data (Horai and Simmons 1972), we used ρ of 2940 kg/m^3 as assumed by Bandfield et al. (2011). The specific heat and thermal conductivity were derived from the sample data as follows:

$$c_p = -154.9 + 4.983T - 0.008207T^2 + 0.000005192T^3 [\mathrm{J/(kgK)}] \quad (4)$$

$$K = \rho c_p \left(\frac{1}{3.14\times10^5 + 3.78\times10^3 T} \right) [\mathrm{W/(mK)}] \quad (5)$$

For regolith, Vasavada et al. (2012) found that the nighttime variation in the temperature measured by Diviner fits the regolith density model which increases exponentially with depth as

$$\rho(z) = \rho_d - (\rho_d - \rho_s) e^{-\frac{z}{H}} \quad (6)$$

where ρ_s is the surficial density, and ρ_d is the density at $z \gg H$. Here, we assumed ρ_s of 1,100 kg/m^3 (Hayne et al. 2017) and ρ_d of 1,800 kg/m^3 (Carrier et al. 1991). Note that the regolith was assumed to have an H-parameter of 7 cm as the lunar average (Hayne et al. 2017). In our simulation, the heat capacity of the regolith depended on its temperature following a polynomial function derived by Hayne et al. (2017) from the data by Hemingway et al. (1981) and Ledlow et al. (1992) as follows:

$$c_p = -3.6125 + 2.7431T + 2.3616T^2 - 1.2340T^3 + 8.9093T^4 [\mathrm{J/(kgK)}] \quad (7)$$

In addition, we used the thermal conductivity model derived by Hayne et al. (2017) from the experimental data of Fountain and West (1970) as

$$K = \left(K_d - (K_d - K_s) \frac{\rho_d - \rho}{\rho_s - \rho} \right) \left(1 + 2.7 \left(\frac{T}{350} \right)^3 \right) [\mathrm{W/(mK)}] \quad (8)$$

where K_s and K_d are the conductivity at the surface and depth, respectively.

Result

Temperature curves in HSD

Figure 4 shows the equatorial brightness temperature curves derived from HSD. In the morning, the lunar temperature rapidly increases from approximately 100 K to over 300 K. Owing to dynamic range limitations, the radiance measured by AHI is saturated from 8 to 16 H. The saturation level ranges from 318 to 328 K, depending on the bands. After 16 H, the lunar surface cools down quickly. This rapid temperature variation around sunset and sunrise results in large standard deviations for values binned at every 0.5 H. However, it should be noted that each temperature value (black points in Fig. 4) is statistically significant on the dayside because its signal-to-noise ratio (S/N) is 10 or even higher. All the analyzed pixels were located within 10°N–10°S, and their emission angle was lower than 10°; therefore, the effect of emission angles on brightness temperatures is smaller than 1 K (Bandfield et al. 2015). In addition, the shape of the temperature curve in each band is asymmetric between the morning and evening, and the evening side has brightness temperatures higher than that of the morning side, notably in bands 13–16. This asymmetry indicates that the surface temperatures available in HSD are far from the radiative equilibrium condition, supporting the necessity for heat conduction in our simulations.

Even at the nightside, where the S/N is generally low, HSD at wavelengths longer than 10 μm can be used by stacking pixel values. The nightside data in Fig. 4 were obtained from 42 lunar images selected by visual inspection to avoid high noise of broad PSF from the nearby Earth or lunar dayside. Although most brightness temperature values in the nightside are not statistically significant in all bands because of their low S/N, the noise can be reduced greatly by binning pixel values at every 0.5 H in some bands. It should be noted that both positive and

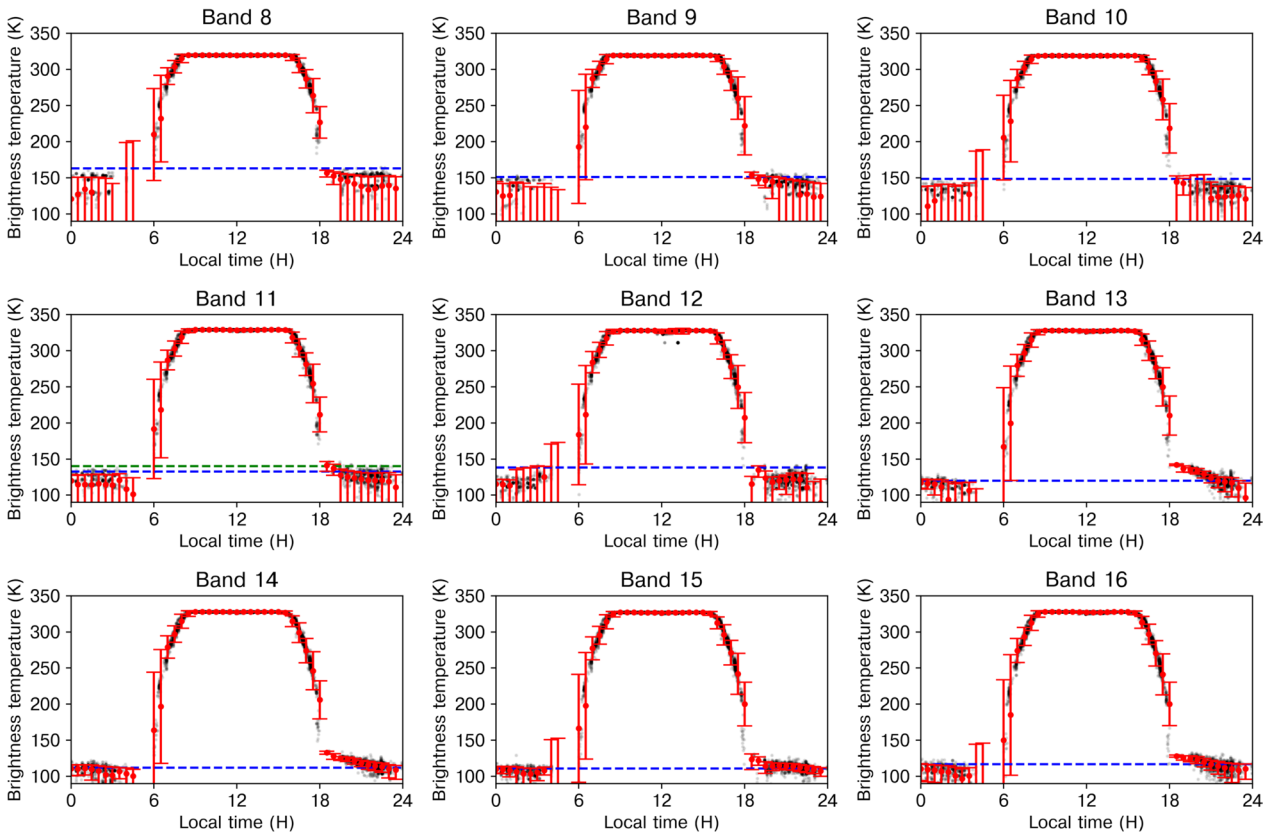

Fig. 4 The brightness temperature curves from HSD at bands 8–16. The gray dots show the brightness temperature in each pixel. The red points with error bars are the average values with standard deviations at every 0.5 H bin. The blue dashed lines indicate the noise level of AHI. The green dashed line in band 11 indicates the noise level of channel 5 of Diviner

negative radiances were included in the averaging procedure. For bands 8–12 with wavelengths shorter than 10 μm, only bins immediately after sunset have standard deviations smaller than the average, and it is difficult to estimate brightness temperatures during the night. Consequently, the radiances of the pixels on the nightside are often negative. Hence, although the black points on the nightside appear crowded in Fig. 4, the standard deviation is still large for bands 8–12. In contrast, the binning procedure is effective for bands 13–16. The brightness temperatures equivalent to the noise in these bands are lower than those in the others; therefore, the mean value is statistically significant. Except for a few hours before sunrise, we can draw the brightness temperature curves for wavelengths longer than 10 μm.

In the morning and evening, the brightness temperature measured by AHI is consistent with that measured by Diviner. Figure 5 shows the compilation of nadir observations of brightness temperatures at AHI band 11 (8.40–8.78 μm) and Diviner channel 5 (8.38–8.68 μm). The HSD temperature shown in Fig. 5 is located where the emission angle is smaller than 5° and the latitude

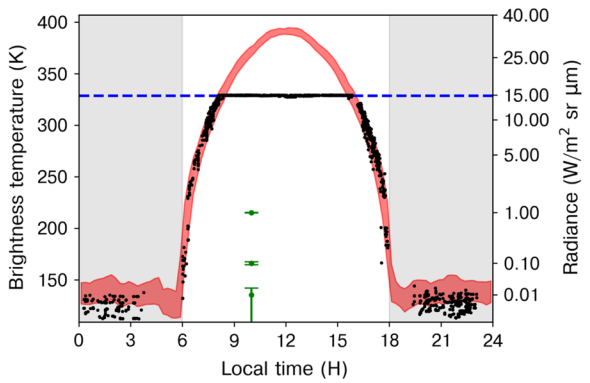

Fig. 5 Comparison of the equatorial brightness temperature measured by AHI at band 11 with Diviner GCP at channel 5. The gray and white areas correspond to the nightside and dayside, respectively. The red area shows the time variation of average brightness with a standard deviation range of Diviner GCP from 5°N to 5°S. The black points are the brightness temperatures of the HSD pixels which correspond to lunar latitude from 5°N to 5°S and emission angle smaller than 5°. Note that HSD is saturated at the blue dashed line. Each green bar indicates the background noise level from the broad PSF at the radiance of 0.01, 0.1, and 1 W/m^2/sr/μm

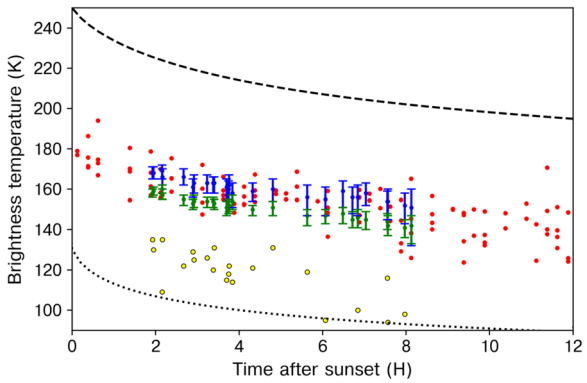

Fig. 6 Brightness temperatures at Tycho crater in the nightside. The red points are the brightness temperatures at the latitude of 43.0°–43.5°S and longitude of 11.0°–11.5°E in Diviner GCP at channel 5. The blue and green points are the brightness temperatures at the center of Tycho crater in HSD at bands 11 and 14, respectively. The error bars are estimated from the background noise level in each image. The black dashed and dotted lines show surface temperature models of lunar rock and regolith at the latitude of 43°S, respectively. The yellow points are the best-fit regolith temperatures in our analysis

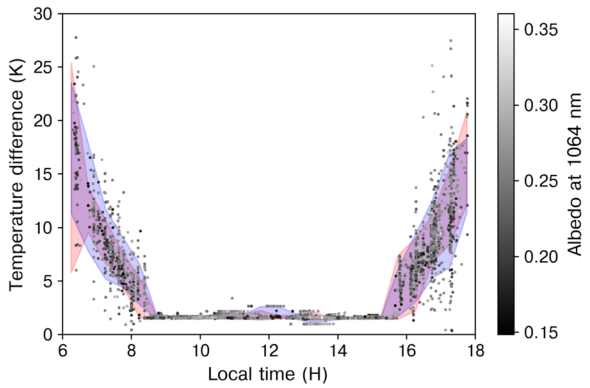

Fig. 7 The difference in brightness temperatures between bands 11 and 15. The color of each point corresponds to albedo at the wavelength of 1064 nm measured by LOLA. The red and blue shades show the range of a standard deviation in the mare and highland regions, respectively. There is no trend from 8 to 16 H due to the saturation

ranges from 5°N to 5°S. The range of the average brightness temperature with a standard deviation of the Diviner data from 5°N to 5°S are shown in Fig. 5. The Diviner data are from the Global Cumulative Product (GCP) available at the Planetary Data System, which is composed of bins of 0.5° latitude and longitude and 0.25 H of local time (Williams et al. 2017). Except for the saturated values around noon, the HSD temperatures are almost within the range of the Diviner data in both the morning and evening.

In contrast, the equatorial temperature range of Diviner GCP is slightly higher than that of HSD on the equator at night. Even though the noise of HSD is large at the nightside, there is an apparent distinction between the temperatures of HSD and Diviner GCP from 22 to 1 H (Fig. 5). This distinction is probably attributed to the noise of Diviner channel 5, which is higher than that of AHI band 11. In the 8.5-μm wavelength, the noise-equivalent temperature of Diviner is around 200 K, and the temperature accuracy exceeds 10 K below 170 K (Paige et al. 2010), indicating a higher sensitivity of AHI than Diviner at low temperatures (Fig. 4).

One exception is the nighttime temperatures of HSD at bright points, which show good agreement with those of the Diviner data. Pixels of some craters, such as Tycho (Fig. 3b), have higher radiances than the lunar average. Most of these pixels have statistically significant values, with their S/N of 3 or larger. For example, the temperature of Tycho crater ranges from 150 to 170 K in band 11 of AHI (Fig. 6), which matches well with that of Diviner GCP.

Anisothermality

The brightness temperature is higher in the morning and evening at shorter wavelengths than at longer wavelengths, as described previously in the "Anisothermality Model" section. Figure 7 shows the brightness temperature difference between band 11 (8.40–8.78 μm) and 15 (11.90–12.86 μm) at every pixel whose radiance values exceed three times the noise level from the broad PSFs at both bands. It should also be noted that bands 14 and 15 were mainly used in our analysis because their noise levels are the lowest. The subtraction of the brightness temperature at band 15 from that at band 11 becomes positive at almost all points. It ranges from 2 to 16 K on average, depending on the solar incident angle. The difference in other local times decreases from noon to sunrise and vice versa in the evening. In addition, the distribution of the scatters as shown in Fig. 7 is asymmetric between the morning and evening, indicating the effects of thermal inertia. Similar trends are also observed for other combinations of bands. These trends are the same as those measured by Diviner at different wavelengths. The brightness temperatures in channels 4 (8.1–8.4 μm) and 7 (25–41 μm) of Diviner differ by 44 K in the early morning (Bandfield et al. 2015), higher than our result probably due to the larger wavelength gap between the two channels.

Daytime anisothermality has no clear correlation with the albedo value. As seen in Fig. 7, the distribution of the scatterers is independent of their albedo value measured

at 1064 nm by LOLA. Furthermore, by dividing the point locations into mare and highland with an albedo threshold of 0.2, we attempt to observe the brightness temperature difference between the mare and highland, but no obvious separation is found at every 0.5 H. This result supports an almost homogeneous distribution of anisothermality over the whole Moon, as the Diviner measurement has already reported (Bandfield et al. 2015).

Anisothermality between different bands is also present at the equator on the nightside. As seen in Fig. 4, the brightness temperatures in the bin of 19 H in local time are 149^{+6}_{-9}, 137^{+6}_{-10}, and 128^{+3}_{-4} K in bands 9, 11, and 15, respectively, where the superscript and subscript suffixes show the upper and lower errors, respectively. These values demonstrate that the equatorial brightness temperature tends to be lower at longer wavelengths. As the similar trend in the dayside, this feature supports the mixture of various temperatures in the field of view, even at the nightside on an average.

The anisothermality of the nightside is characterized by its locality. Figure 3b shows that the image of an almost new Moon in band 14 contains bright pixels corresponding to fresh craters such as Tycho, Aristarchus, Copernicus, and Zucchius. Mare regions also have radiances higher than the average. At such locations, the brightness temperature difference among the bands is confirmed. For example, the comparison of brightness temperatures between bands 11 and 14 in Fig. 6 reveals the anisothermality at Tycho crater even after midnight.

Discussion

Roughness

The increase in anisothermality with the solar incidence angle on the dayside indicates the contribution of the surface roughness to infrared emission. The mixing of illuminated and shadowed surfaces results in a variety of surficial temperatures within a pixel, which increases with incidence angle (Fig. 7).

The similarity of the anisothermality distribution between highland and mare in Fig. 7 indicates that the lunar roughness is almost independent of the geological settings on the Moon on a scale from millimeters to centimeters. Although topographic roughness at the kilometric scale is highly correlated with geology, roughness becomes spatially less heterogeneous at smaller scales (Kreslavsky et al. 2013). The spatial scale of the roughness sensitive to the infrared spectrum corresponds to the thermal isolation length. If the distance between the sunlit and shadowed surfaces is long enough, the temperature heterogeneity inside the medium diffuses insufficiently. This diffusive scale is the thermal isolation length. For media with low thermal inertia such as lunar regolith, Bandfield et al. (2015) estimated that the thermal isolation length is shorter than centimeters based on the two-dimensional thermal diffusion model. Thus, Fig. 7 suggests that mare and highland have no significant difference in surficial roughness at centimetric or smaller scales. This similarity is probably due to the uniform bombardment of numerous micrometeorites almost everywhere on the Moon. This dominance of micrometeorite collisions on small-scale surface modifications has been observed as the equilibrium population of craters smaller than 300 m in diameter (Melosh 1989).

For further interpretation of the lunar image seen by AHI, we quantitatively estimate the roughness contribution to the lunar radiance by changing the RMS slope angle of the surface, θ_0. Figure 8a and b shows examples of the observed and simulated lunar images of 2020/05/30 21:10 at band 15. Our simulation with θ_0 of 18° yields radiances similar to the observation. As shown in Fig. 8c, the difference between (a) and (b) is within 10% at incident angles of 70° or less. Otherwise, the simulated image is darker than the observation by more than 10%.

The above roughness value that explains the observation is consistent with the photometric roughness observed locally at Apollo landing sites. At pixels where the incident angle is less than 70°, the radiance simulated with θ_0 of 16°–20° matches the observed radiance within 10%. Based on a photometric approach with Apollo Surface Closeup Camera pictures, Helfenstein and Shepard (1999) estimated that θ_0 ranged from 15° to 28° and 5.4° to 22° at roughness baseline lengths of 0.85 and 8.5 mm, respectively. However, θ_0 was larger than 48° and smaller than 3.8° at the 0.085- and 85-mm scales, respectively. Therefore, the roughness observed in HSD is consistent with that measured locally at the scale between millimeters and centimeters. This scale agrees with the length capable of remaining thermally isolated in previous numerical models (Bandfield et al. 2015).

In our simulation, the radiance near the dayside terminator is always darker than that of HSD, probably because of the limitation of the statistical roughness model. On non-flat terrain, a surface absorbs energy by direct illumination from the sun and radiation scattered and emitted from other surfaces. Such secondary illumination also warms the surface and is known as self-heating. Our thermal conduction model considers only the absorption of the direct flux from the sun and ignores the self-heating effect to avoid a high computational cost. Ignoring self-heating might underestimate the radiance value, as Davidsson et al. (2015) demonstrated that self-heating increases the surface temperature of shadowed facets to 100–200 K at an incident angle of 80°.

Moreover, the ratio of cast shadows predicted by the statistical model is perhaps larger than the real value, resulting in the underestimation of radiance in our

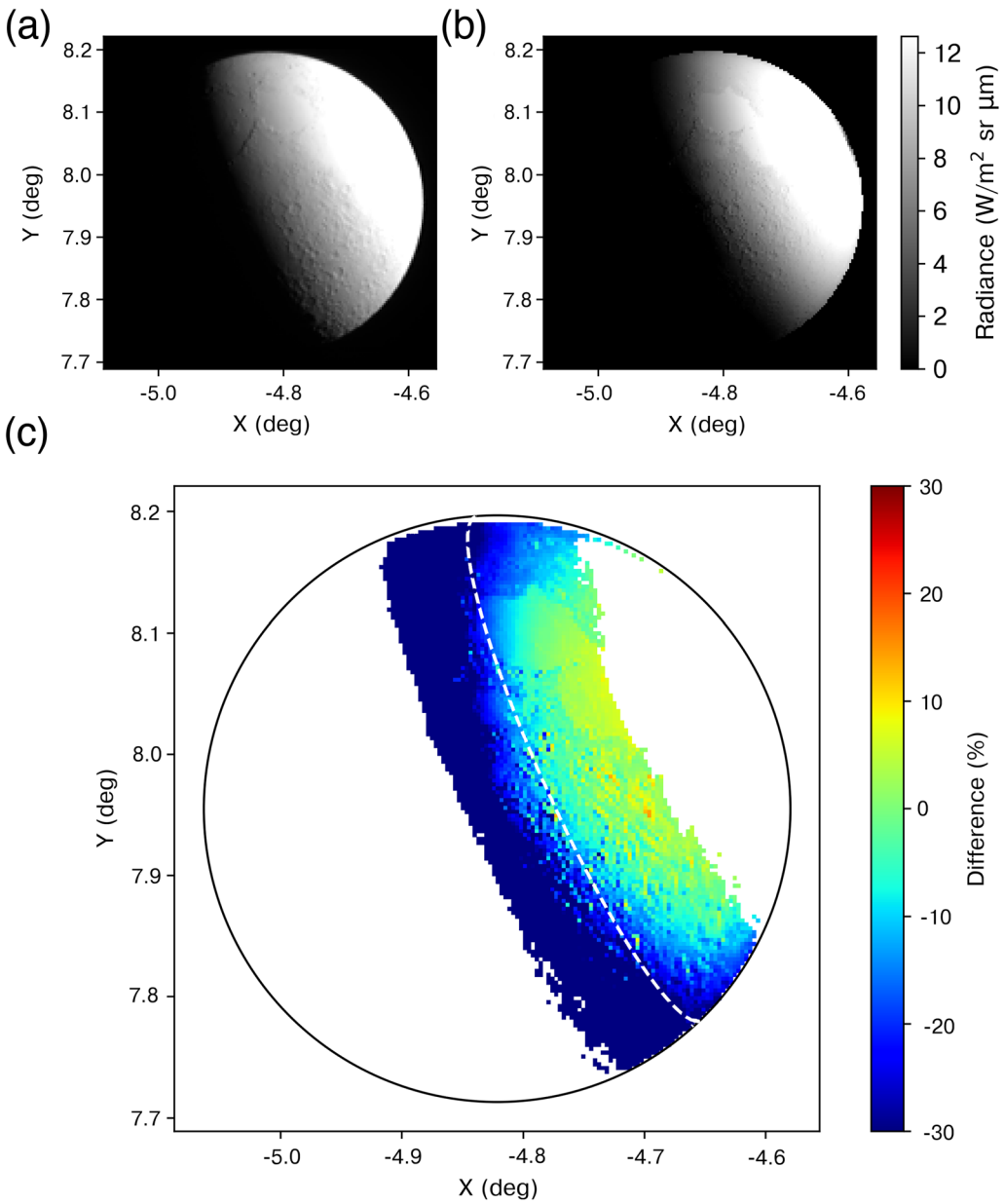

Fig. 8 The lunar images of **a** observation and **b** simulation with θ_0 of 18° in band 15 at 2020/05/30 21:10, respectively. **c** The difference between observation and our simulation in percent. The white area corresponds to space, saturated pixels, or nightside. The white dashed line is located where the incident angle is 70°

simulation. Davidsson et al. (2015) compared a statistical model to a realistic simulation. Their realistic simulation included radiative equilibrium and self-heating on rough terrain, digitally composed of numerous flat facets with various slopes. When the solar incident angle was 80°, they predicted that the radiance was fainter in the statistical model than in the realistic one. This difference was highly dependent on θ_0. For instance, the difference reached 5 and 40% in the case of θ_0 of 5° and 20°, respectively. However, when the solar incident angle was 60°, the absolute difference was generally smaller than 10% at 10 μm. Therefore, it is evident that our simulation using the statistical roughness model is a first-order approximation, except for the time just before sunset and after sunrise.

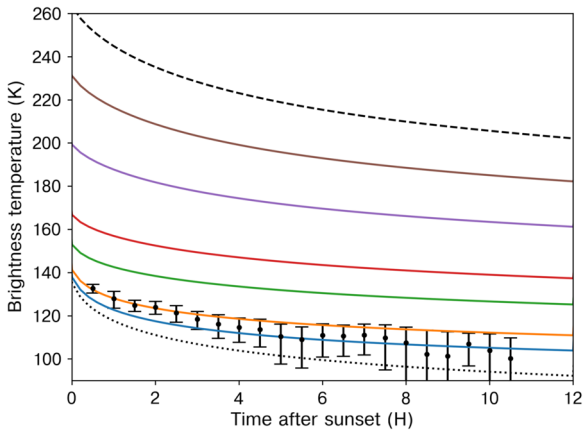

Fig. 9 Average equatorial brightness temperatures at band 14 in the nightside. Black points with error bars are the average values with standard deviations at every 0.5 H bin. The black dashed and dotted lines show surface temperature models of lunar rock and regolith at the equator, respectively. The blue, orange, green, red, purple, and brown solid lines are brightness temperature curves of mixture models with rock ratios of 0.2, 0.5, 2, 5, 20, and 50%

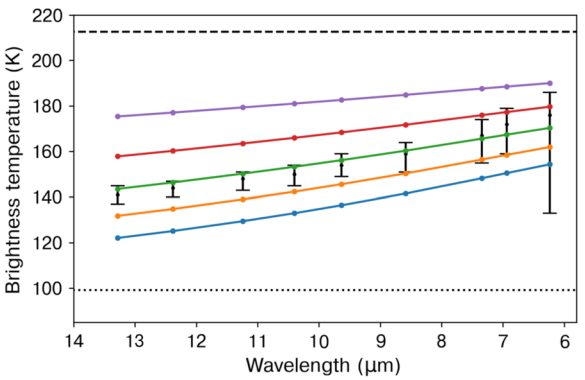

Fig. 10 Anisothermality of Tycho crater in the image taken on 2021/02/13 16:30, with a corresponding local time of 0.5 H. The black points are the brightness temperatures at the center of Tycho crater in HSD at every band. The black error bars are estimated from the background noise level in each image. The black dashed and dotted lines show surface temperature models of lunar rock and regolith in Tycho crater at the same local time, respectively. The blue, orange, green, red, and purple solid lines are predicted brightness temperatures of mixture models with rock ratios of 2.5, 5, 10, 20, and 40%

Rock mixture effect on the nightside

The nighttime anisothermality, shown in Figs. 4 and 6, cannot be attributed to roughness. The effect of topographic roughness at the thermal isolation length scale becomes insignificant after sunset. Furthermore, even at a much longer scale than that tested by Bandfield et al. (2015), such a difference is negligible after at least 20 H. For instance, at the 17-m scale, the median slope of the lunar surface is 2.0°–7.6° (Rosenburg et al. 2011). For such slope angles, our simulation suggests that the temperature difference between the western and eastern sides is less than 3K at a local time of 20 H.

Instead, the brightness temperatures at night reflect a mixture of rock and regolith. Typically, the nighttime temperature of the rock is higher than that of the regolith owing to the high thermal inertia of the rocky material. For example, our simulation predicts that the midnight temperature of the rock is as high as 215 K, in contrast to that of the regolith at 100 K. The observed brightness temperature curve is drawn between the rock and regolith temperatures. Figure 9 shows that the binned brightness temperature observed by AHI at band 14 is slightly higher than that of the regolith. In addition, the brightness temperatures of Tycho crater are distributed between those of the rock and regolith at any bands (Fig. 10). Thus, nighttime brightness temperatures cannot be explained only by radiance from the cold regolith, suggesting the presence of rocks.

By modeling the brightness temperature of the mixture of rock and regolith, only a small amount of rock is even detectable from HSD. The Planck radiance from the hot rock is much more intensive than that from the cold regolith; therefore, the non-linear mixture of temperatures is dominated by the contribution of rocks to the total radiance. For example, in contrast to the regolith temperature of 100 K at midnight, the equatorial brightness temperatures in band 14 are 155, 131, and 116K, with rock concentrations of 10, 2, and 0.5%, respectively.

The comparison between the mixture model and observations at the nightside indicates that the equatorial rock abundance ranges from 0.18 to 0.48%. In this estimation, the brightness temperature curves at bands 14 and 15 were used because the noise levels in these bands are minimal. Additionally, we excluded the values before 20 H to eliminate the influence of roughness. As a result, models with rock abundance of 0.18–0.48 and 0.10–0.55% match over 70% of binned values within the standard deviation at bands 14 and 15, respectively. According to the spatial distribution of rock abundance derived from the Diviner measurements (Bandfield et al. 2011), the mean value ranged from 0.01 to 0.72% in the corresponding area to around nadir in the AHI images. Although wavelengths longer than the AHI coverage were used in their analysis, this consistency strongly supports the availability of lunar radiance around 10-μm wavelengths for rock abundance estimation.

Furthermore, a pixel at Tycho crater brighter than the average reflects an elevated rock abundance. Figure 10 compares the rock mixture model with the brightness temperatures measured at every band at 2021/02/13

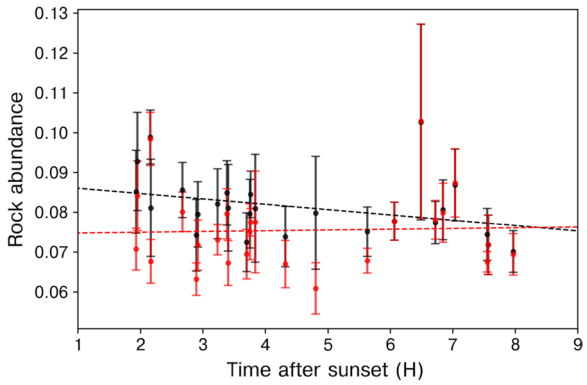

Fig. 11 The rock abundance at Tycho crater and its relationship with local time after sunset. The black and red points show estimates based on the assumption of *H* of 7 cm and best-fit regolith temperatures. The black and red dashed lines are linear regressions for both cases with correlation coefficients of -0.34 and 0.04, respectively. Each error bar corresponds to a standard deviation of rock abundance estimated in all the analyzed AHI bands

16:30. This figure shows that the rock ratio of Tycho crater is more than an order of magnitude higher than the equatorial value. We employ this procedure for images whose S/N within Tycho crater exceeds one in 7 bands or more and derive rock abundances in all images.

According to our analysis of Tycho crater, the rock abundance is higher than that of the lunar equator, which is consistent with the Diviner observations. Furthermore, it is suggested that the regolith is hotter than the lunar average. Here, we fit the rock abundance by minimizing the residuals of the brightness temperatures between the observations and simulations. If the regolith temperature is modeled with *H* of 7 cm, the rock abundance fitted to the observed brightness temperatures decreases slightly with time after sunset (black points in Fig. 11). This indicates that the assumption of the Tycho regolith temperature being as cold as the global average is unreasonable. However, if we fit both rock abundance and regolith temperature itself, such an implausible trend can be reduced (red points in Fig. 11). As a result, the correlation coefficient between rock abundance and time shifts from -0.34 to 0.04. This procedure derives rock abundance with a mean of 6.1–10.3%. This value agrees with the estimation from the Diviner measurements which has the mean value of $7.8 \pm 5.7\%$ inside Tycho crater (Bandfield et al. 2011). Additionally, the fitted regolith temperatures inside Tycho are mostly higher than those predicted using the global average *H*-parameter. The yellow points in Fig. 6 correspond to the regolith temperatures of the best-fit model. These warm temperatures are consistent with the high thermal inertia of the Tycho regolith reported by Hayne et al. (2017).

Young craters, such as Tycho, are known to have elevated rock abundances due to the low level of regolith maturation (Bandfield et al. 2011). This characteristic is also reflected in HSD, perhaps similar to the Copernican craters: Aristarchus, Copernicus, and Zucchius (Fig. 3). In addition, Bandfield et al. (2011) also reported that small maria craters, typically with diameters of hundreds of meters, expose more abundant rock than highlands. In HSD, mare regions have higher radiances than highlands, showing the same trend as previous estimates (Fig. 3).

Effect of parameter assumptions on the derived values

A lunar emissivity of 0.95 was used throughout our analysis, and the results are little dependent on this assumption. Based on the RELAB data of lunar soils (Pieters 1983), the emissivities of the Apollo samples spanned between 0.94 and 0.99 at 8–16 μm wavelengths. However, the infrared radiance from a gray body is subject to temperature more extensively than the slight variation in emissivity. For example, the radiance from a 300-K surface with an emissivity of 0.99 is equivalent to the surface temperature and emissivity of 302 K and 0.95 in band 11. This temperature difference is much smaller than the range of Diviner GCP (Fig. 5).

The influence of the assumed parameters on the estimated rock abundance is also evaluated in our analysis. The physical properties of rocks in either highland or mare are assumed to be the same as the lunar basalt sample (Horai and Simmons 1972), while highland rocks generally have higher albedo and lower density than mare basalts (Kiefer et al. 2012). Thus, the highland rock temperature can be lower than our estimates by up to 5 K at midnight. Accordingly, the derived rock abundance increases by 0.05 and 1.5% in the equatorial region and Tycho crater, respectively. Finally, we state that this assumption is required to compare the Diviner rock abundance because Bandfield et al. (2011) used the same parameters for their estimation.

Utility of HSD for further planetary science

The quality of HSD is sufficiently high to be utilized in planetary science and future explorations. Despite the low spatial resolution, temperature detection by AHI is accurate, as clearly shown in Fig. 5. In contrast to Diviner, which loses its sensitivity below 140 K at 8.5-μm channels, AHI can detect low radiance from cold surfaces on the nightside. Additionally, the wavelength coverage of AHI overlaps with that of other spaceborne observations. Therefore, AHI is useful for calibrating these instruments during their swing-bys with the Earth and other planets. Not only the Moon but also planets such as Venus, Mercury, Mars, and Jupiter are included in HSD with a size of a few pixels (Fig. 12). Thus, even if the target is as cold as

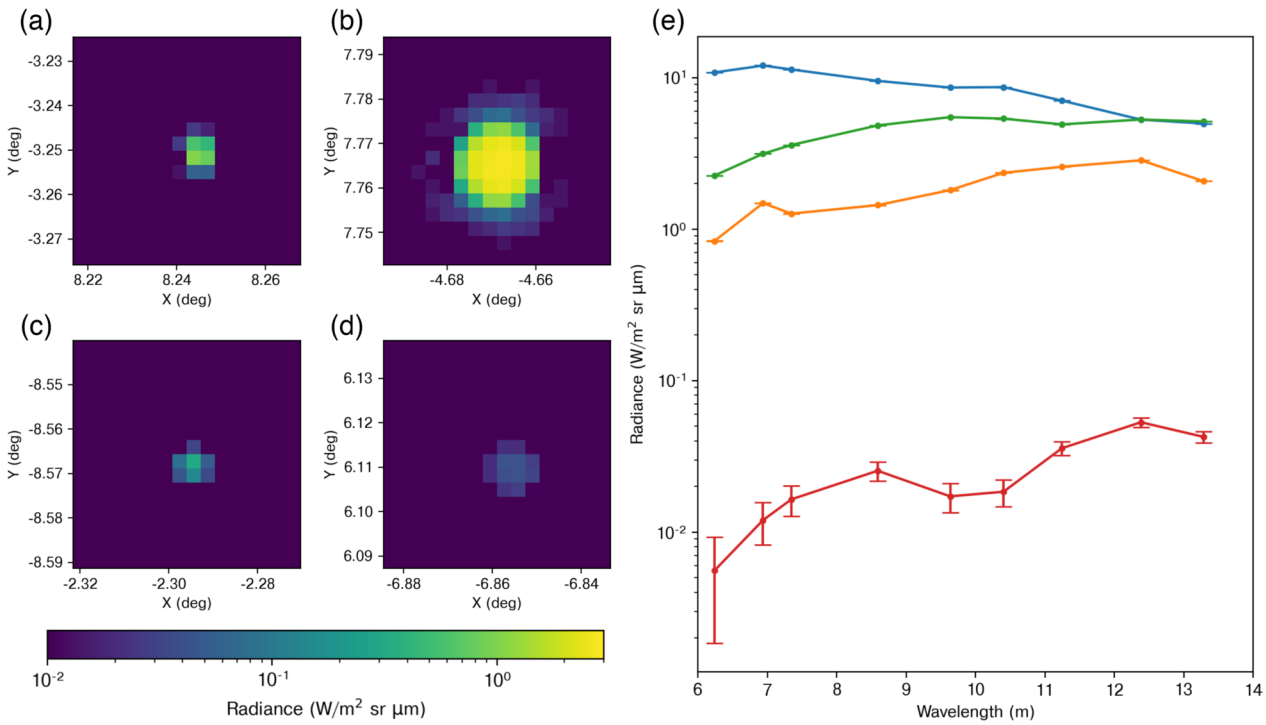

Fig. 12 Examples of planetary images at band 14 of AHI: **a** Mercury, **b** Venus, **c** Mars, and **d** Jupiter. The images were taken from data at 2016/08/29 16:20, 2017/03/30 13:40, 2017/01/01 18:20, and 2016/03/11 02:10, respectively. **e** The disk-normalized infrared spectrum of planets. The blue, orange, green, and red lines correspond to **a**, **b**, **c**, **d**, respectively. The error bars show the background noise level in the images

150 K, the disk-normalized radiance of those planets covered by AHI can be used for interplanetary calibrations.

After the thermal spectrum is reconstructed, the compositional features of the lunar surface shall be retrieved. Unfortunately, however, further discussions are difficult with the existing HSD because of count saturation. The lunar radiance in HSD is only available for the morning, evening, and night when physical properties other than composition significantly affect the infrared spectrum. Because a slight variation in emissivity must be measured for compositional constraints, these properties make it difficult to discuss a few percent difference in emissivity among bands.

However, if the unsaturated lunar image of noontime is taken by shifting the dynamic range of AHI, the uncertainty of thermal radiance can be reduced from the high incidence angle cases in three aspects. First, the roughness effect on anisothermality will become small enough because the variation of temperatures in a field of view decreases at a low incident angle. The Diviner measurements show that the brightness temperature difference between channels 4 and 7 is only 5 K at incident angles lower than 30° (Williams et al. 2017). In addition, Bandfield et al. (2015) demonstrated that the anisothermality modeled with the statistical roughness differs from the observed anisothermality by less than 2 K at an incident angle lower than 30°. This difference corresponds to the radiance prediction error of only 4% at 350K in band 8 of AHI.

Second, the uncertainty of the albedo decreases at incident angles lower than 30°. The albedo value is often regarded to be dependent on the solar incident angle in estimating the lunar surface temperature (Hayne et al. 2017; Williams et al. 2017; Zhang et al. 2019). Laboratory measurements empirically showed that the reflectance of Apollo samples around 1 µm increased with the incident angle (Birkebak et al. 1970). Based on these data, Keihm (1984) expressed the albedo as a polynomial of the solar incident angle. In addition, Vasavada et al. (2012) updated the constants in the formulation by comparing the radiative equilibrium model with the daytime temperatures measured by Diviner. However, we must pay attention to the limitation of the reflectance measurements by Birkebak et al. (1970), where the incident angle is lower than 60°. In addition, the albedo estimated by Vasavada et al. (2012) is perhaps higher than that on a flat surface because their model implicitly includes a roughness effect. The large portion of the cast shadow at a high incidence angle reduces infrared radiation, increasing the apparent albedo. As a result, the albedo values in the

empirical formulation by Keihm (1984) and Vasavada et al. (2012) reach 0.50 and 0.62 at an incident angle of 80°. Thus, the uncertainty of the albedo around the terminators is larger than 20%. However, at an incident angle smaller than 30°, the albedo differs by only 4% between the two models.

Third, the computational cost of the surface temperature is much lower for the case at noon than that at morning and evening. Between local times of 8 H and 16 H, the radiative equilibrium model can approximate the surface temperature within a 1-K error. Without the temporal development of heat conduction, the surface temperature prediction with the radiative equilibrium model requires a computation cost of orders of magnitude lower than that with the heat conduction model. Instead, we can incorporate the roughness effect with digital facets, more accurately than the statistical model (Davidsson et al. 2015).

Such an ideal HSD is useful for discussing the spatial variation of compositions, such as the upper limit of water concentration on the Moon. Band 8 of AHI covers the wavelength of the 6-μm emission peak of water. In contrast to the 3-μm feature which cannot distinguish between water molecules and hydroxyl compounds, this wavelength is helpful for directly investigating water distribution for future human explorations. This peak has already been observed by the SOFIA telescope (Honniball et al. 2021), but the data are limited only to the periphery of Clavius crater. Based on the empirical relationship derived from the laboratory measurements of 6-μm absorption of water-bearing glass beads (Honniball et al. 2021; Li and Milliken 2017), the 0.05 wt% water content will be identified as a 5% emission excess at 6 μm. If AHI observes this peak in band 8, the radiance excess is reduced to 0.5% owing to its broad bandwidth. Thus, for the detection of 0.05 wt% water, the lunar infrared radiance without water must be modeled with an accuracy of less than a few tenths percent. Considering the 4% error by the albedo and roughness model around noon, it is necessary to stack hundreds of differences between unsaturated images and simulations to constrain still-ambiguous water distribution. Neutron detection by LRO indicated that the water equivalent hydrogen in the top 1-m layer reaches more than 0.5 wt % in the polar region (Sanin et al. 2017). Contrarily, the 3-μm reflectance measurement by M^3 onboard Chandrayaan-1 showed the OH/H_2O content increased with latitude up to 0.05–0.075 wt% (Li and Milliken 2017). In addition, the spatial resolution of HSD is higher than the size of Clavius crater (Honniball et al. 2021), indicating the possibility of mapping the water distribution on the Moon. Although the infrared emission reflects only the composition of the top surface, the AHI observation of the full Moons without saturation can impose another constraint on the upper-limit map of water concentration on the Moon.

Conclusion

The Japanese meteorological satellite Himawari-8 proves useful for lunar science for the first time. Although the spatial resolution is low, the infrared radiance measured by AHI is consistent with that measured by the LRO Diviner radiometer. Except for noontime, the brightness temperature curves can be drawn for all nine infrared bands. Our analysis also confirms anisothermality which indicates the non-linear mixing of thermal radiation from various temperatures as previously reported.

In the morning and evening, the surface roughness of the Moon causes this anisothermality. The lunar terrain is composed of various millimeter-scale slopes, as observed in in situ and remote sensing measurements, causing temperature differences between the west- and east-facing surfaces. By incorporating the statistical roughness model with the RMS mean slope angle of the Apollo landing sites, our simulations agree with the HSD within 10% except for the dayside terminators. Furthermore, nighttime anisothermality reflects the abundance of conductive rocks within each pixel. Modeling the surface temperature mixtures of lunar rock and regolith, the rock concentrations are estimated as 0.18–0.48 and 6.1–10.3% at the equator (10°N–10°S) and Tycho crater, respectively. These values are consistent with the constraints from the Diviner observations.

Currently, unsaturated dayside pixels are limited to local times when surficial roughness produces uncertainties too large to discuss slight emissivity variations. However, if the saturation level of AHI can be higher than 3 times the present one by changing the exposure time, and if the unsaturated data are obtained for the noontime, the uncertainties of shadows and albedo will be significantly reduced, and the computational cost for numerical modeling will be much less expensive. As a result, stacking hundreds of unsaturated data will possibly enable the detection of a slight variation in emissivity. While AHI does not have as many bands around 8 μm as Diviner, band-11 observation can provide complementary data for the Diviner constraints on Christiansen feature. Furthermore, the AHI observation at band 8 may enable mapping the upper limit of the lunar water contents on the surficial layer. As a result, such stacking will possibly enable imposing constraints on lunar water emissions at 6-μm bands. It takes only 0.4 s to take a full lunar image with AHI; thus, campaign observation of the Moon with Himawari-8 only for a few minutes can provide essential data for lunar

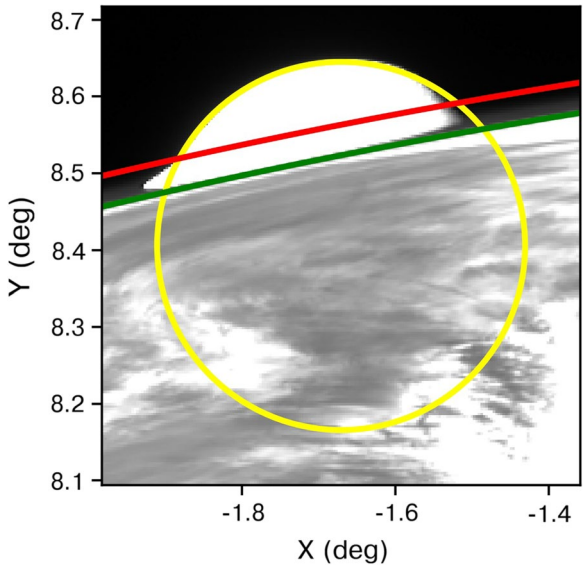

Fig. 13 The lunar image of 2017/09/10 05:40 at band 14 with the lunar rim bent by the terrestrial atmosphere. The yellow circle is the lunar rim determined by fitting a circle. The green line is the Earth's rim. The red line is the rim of the eliminated area from the following analysis, that is, a circle with a radius of 100.45% of the Earth. The lunar pixels between the red and green lines are refracted by the terrestrial atmosphere

science. In addition, because the AHI image often includes other planets such as Mercury, Venus, Mars, and Jupiter, HSD is also a valuable data source for the occasional monitoring of these planets. Thus, Himawari-8 has great potential as a space telescope for further discussion of planetary science.

Appendix

HSD pixel positions

We determine the lunar center in each image to link the AHI image pixels to longitudes and latitudes on the Moon. We can estimate the lunar position roughly with SPICE. However, the estimated center is sometimes far from the real one by almost ten pixels, possibly because of the low precision of the scanning time. To overcome this problem, we select lunar rim candidates by determining the position of the maximum derivative of the radiance along the x- and y-axes. We then fit a circle with an apparent lunar diameter to the candidates. In some cases, especially around new Moons, the candidates include false detections of the rim owing to the low level of S/N ratio. We eliminate the candidate farthest from the fitted circle and fit it again to avoid misfitting. We determine the lunar center by iteratively conducting this process until all remaining candidates match the fitted circle within one pixel. Note that the criterion of 1 pixel is sufficient because the lunar spatial resolution of 23 km in the AHI images is larger than the lunar topographic relief spanning 19.81 km (Araki et al. 2009). Using the determined lunar position on the image, the lunar orientation is calculated using SPICE to link each pixel to the longitude and latitude on the Moon.

The lunar area near the Earth is affected by terrestrial atmospheric refraction and thus should be excluded from the analysis. We selected 8 images (2017/09/10 05:40, 2018/01/23 20:20, 2018/04/02 03:30, 2018/07/31 04:50, 2018/10/20 23:40, 2020/04/06 01:00, 2021/07/02 08:20, 2021/09/23 03:40) when the lunar rim looks distorted by the atmosphere (Fig. 13). As described above, we first find the lunar rim candidates and the fitted circle similarly. Then, the maximum distance from the Earth's center is calculated for candidate pixels that are more than one pixel away from the circle. As a result, it is found that the area within a distance of 0.45% of the Earth's radius from the Earth's rim is affected by atmospheric refraction, and this area was eliminated from the latter analysis.

Statistical roughness model

We employ a statistical roughness model that follows Gaussian slope distribution based on previous models. In this model, we first consider the temperature distribution on rough terrain. Then, the emission is corrected with approximate fractions of sunlit and shadows from every solar and observer direction.

We prepare a dataset of the surface temperature on a facet for slopes of 0°–90° at 2° intervals and azimuth orientations of 0°–360° at 10° intervals using a one-dimensional thermal conductive model. Using this dataset, the mixture of the Planck radiation of rough terrain is integrated with the probability weighting of the slope angles. We use the probability function of the simple Gaussian roughness model as,

$$P(\theta) = \frac{\tan\theta}{\tan^2\theta_0}\exp\left(-\frac{\tan^2\theta}{2\tan^2\theta_0}\right) \tag{9}$$

where θ is the slope angle, and θ_0 is the RMS slope angle. This model approximates the Gaussian distribution of unidirectional slope angles in the adirectional form (Shepard et al. 1995). Stereophotogrammetry with Apollo Surface Closeup Camera pictures shows that the submillimeter-scale unidirectional surface slope is described adequately with a simple Gaussian distribution model (Helfenstein and Shepard, 1999). Note that the probability is uniform for all the azimuth orientations. It should also be noted that the LOLA topography data with the maximum spherical harmonic degree and order of 2050 is incorporated to quantify the effect of km-scale relief.

The influence of apparent shadows and sunlit on radiance emission is estimated using a simple shadowing method developed by Hapke (1984) and Smith (1967). In this model, the fraction of cast shadow is assumed to be uniform for all sets of slopes and azimuths of the facets. Combining Eqs. (21) and (24) of Smith (1967), the fraction of the shadowed surface dependent on the solar incident angle, $W(\theta_i)$, can be given as

$$W(\theta_i) = \frac{1-\frac{1}{2}\mathrm{erfc}\left(\frac{1}{\sqrt{2}\tan\theta_i\tan\theta_0}\right)}{\frac{1}{2}\left(\sqrt{\frac{2}{\pi}}\tan\theta_i\tan\theta_0\exp\left(-\frac{1}{2\tan^2\theta_i\tan^2\theta_0}\right)-\mathrm{erfc}\left(\frac{1}{\sqrt{2}\tan\theta_i\tan\theta_0}\right)\right)+1} \tag{10}$$

where erfc denotes the complementary error function. Note that this formulation is only applicable to nadir observations because the effect of the emission direction is not considered.

For observations with non-zero emission angles, the angle between the incidence and emission azimuths influences the fraction of shadows in the field of view, and hence the radiance values. For example, given that the observer is looking from the same direction as the sun, a sunlit side is more apparent than a shadowed one, resulting in higher radiance than the case with the observer looking from the opposite direction. Pixels in the observed images contain wide-ranging combinations of incidence and emission directions; therefore, comparing observed and simulated images requires the incorporation of the effect of viewing orientations. In our numerical models, the fraction of the shadowed surface is expressed simply like that described by Hapke (1984). For locations whose emission angle is larger than the incidence angle, the fraction is

$$\tilde{W} = W(\theta_i)\left(1-\exp\left(-2\tan\left(\frac{\Phi}{2}\right)\right)\right) \tag{11}$$

where Φ is the angle between the incident and emission azimuths. However, for locations whose emission angle is smaller than the incidence angle, the fraction is

$$\tilde{W} = W(\theta_i) - W(\theta_e)\exp\left(-2\tan\left(\frac{\Phi}{2}\right)\right) \tag{12}$$

where θ_e denotes the emission angle. Note that $W(\theta_e)$ in the second term of Eq. (12) is calculated using Eq. (10) by substituting θ_e for θ_i.

Abbreviations

AHI: Advanced Himawari Imager; LRO: Lunar Reconnaissance Orbiter; SOFIA: NASA/DLR Stratospheric Observatory for Infrared Astronomy; TIR: Thermal infrared imager; LIR: Longwave infrared camera; OTES: OSIRIS-REx Thermal Emission Spectrometer; TES: Thermal Emission Spectrometer; Mini-TES: Miniature Thermal Emission Spectrometer; MERTIS: Mercury Radiometer and Thermal Infrared Spectrometer; HIRS: High-Resolution Infrared Radiation Sounder; HSD: Himawari Standard Data; NS: North–south; EW: East–west; PSF: Point spread function; LOLA: Lunar Orbiter Laser Altimeter; RMS: Root mean square; S/N: Signal-to-noise ratio; GCP: Global Cumulative Product.

Acknowledgements

The authors are grateful to Dr. Paul Hayne for providing H-parameter data on the Moon. The authors thank Dr. Yuri Shimaki, Dr. Hauke Hussmann, and Dr. Alexander Stark for fruitful discussions and two anonymous reviewers for their kind and thoughtful comments. We would like to thank Editage (www.editage.com) for English language editing.

Author contributions

GN investigated all the data, established the methodology, and finalized the manuscript. GN and NN wrote the original draft. NN, SS, and SU supervised the content. GN and SU conceptualized the research. All the authors read and approved the final manuscript.

Funding

This work is supported by IGPEES, WINGS Program, the University of Tokyo, and the Publication Committee of National Astronomical Observatory of Japan.

Availability of data and materials

All HSD are collected and provided under the Data Integration and Analysis System (DIAS), which was developed and operated by a project supported by the Ministry of Education, Culture, Sports, Science, and Technology. The LOLA topography, albedo, and the Diviner rock abundance data are open to the public through NASA's PDS Geosciences Node (https://pds-geosciences.wustl.edu/missions/lro/default.htm).

Declarations

Ethics approval and consent to participate

Not applicable.

Consent for publication

Not applicable.

Competing interests

The authors declare that they have no competing interests.

Author details

[1]Department of Earth and Planetary Science, Graduate School of Science, University of Tokyo, Tokyo 113-0033, Japan. [2]National Astronomical Observatory of Japan, Mitaka, Tokyo 181-8588, Japan. [3]The Graduate University for Advanced Studies, SOKENDAI, Hayama, Kanagawa 240-0193, Japan. [4]Institute of Astronomy, Graduate School of Science, The University of Tokyo, 2-21-1 Osawa, Mitaka, Tokyo 181-0015, Japan.

Received: 23 March 2022 Accepted: 9 June 2022
Published online: 04 July 2022

References

Araki H, Tazawa S, Noda H, Ishihara Y, Goossens S, Sasaki S, Kawano N, Kamiya I, Otake H, Oberst J, Shum C (2009) Lunar global shape and polar topography derived from Kaguya-LALT laser altimetry. Science 1979(323):897–900. https://doi.org/10.1126/science.1164146

Bandfield JL (2009) Effects of surface roughness and graybody emissivity on martian thermal infrared spectra. Icarus 202:414–428. https://doi.org/10.1016/j.icarus.2009.03.031

Bandfield JL, Edwards CS (2008) Derivation of martian surface slope characteristics from directional thermal infrared radiometry. Icarus 193:139–157. https://doi.org/10.1016/j.icarus.2007.08.028

Bandfield JL, Ghent RR, Vasavada AR, Paige DA, Lawrence SJ, Robinson MS (2011) Lunar surface rock abundance and regolith fines temperatures derived from LRO Diviner Radiometer data. J Geophys Res. https://doi.org/10.1029/2011JE003866

Bandfield JL, Hayne PO, Williams JP, Greenhagen BT, Paige DA (2015) Lunar surface roughness derived from LRO Diviner Radiometer observations. Icarus 248:357–372. https://doi.org/10.1016/j.icarus.2014.11.009

Bessho K, Date K, Hayashi M, Ikeda A, Imai T, Inoue H, Kumagai Y, Miyakawa T, Murata H, Ohno T, Okuyama A, Oyama R, Sasaki Y, Shimazu Y, Shimoji K, Sumida Y, Suzuki M, Taniguchi H, Tsuchiyama H, Uesawa D, Yokota H, Yoshida R (2016) An introduction to Himawari-8/9—Japan's new-generation geostationary meteorological satellites. J Meteorol Soc Jpn 94:151–183. https://doi.org/10.2151/jmsj.2016-009

Birkebak RC, Cremers CJ, Dawson JP (1970) Directional spectral and total reflectance of lunar material. Proceedings of the Apollo 11 Lunar Science Conference 3, pp. 1993–2000.

Carrier WD, Olhoeft GR, Mendell W (1991) Physical properties of the lunar surface. Lunar Sourcebook: a user's guide to the moon. Cambridge University Press, Cambridge, pp 475–594. (ISBN 0-521-33444-6)

Christensen PR, Bandfield JL, Hamilton VE, Ruff SW, Kieffer HH, Titus TN, Malin MC, Morris RV, Lane MD, Clark RL, Jakosky BM, Mellon MT, Pearl JC, Conrath BJ, Smith MD, Clancy RT, Kuzmin RO, Roush T, Mehall GL, Gorelick N, Bender K, Murray K, Dason S, Greene E, Silverman S, Greenfield M (2001) Mars global surveyor thermal emission spectrometer experiment: investigation description and surface science results. J Geophys Res 106:23823–23871. https://doi.org/10.1029/2000JE001370

Christensen PR, Mehall GL, Silverman SH, Anwar S, Cannon G, Gorelick N, Kheen R, Tourville T, Bates D, Ferry S, Fortuna T, Jeffryes J, O'Donnell W, Peralta R, Wolverton T, Blancy D, Denise R, Rademacher J, Morris RV, Squyres S (2003) Miniature thermal emission spectrometer for the mars exploration rovers. J Geophys Res. https://doi.org/10.1029/2003je002117

Christensen PR, Hamilton VE, Mehall GL, Pelham D, O'Donnell W, Anwar S, Bowles H, Chase S, Fahlgren J, Farkas Z, Fisher T, James O, Kubik I, Lazbin I, Miner M, Rassas M, Schulze L, Shamordola K, Tourville T, West G, Woodward R, Lauretta D (2018) The OSIRIS-REx thermal emission spectrometer (OTES) instrument. Space Sci Rev. https://doi.org/10.1007/s11214-018-0513-6

Conel JE (1969) Infrared emissivities of silicates: experimental results and a cloudy atmosphere model of spectral emission from condensed particulate mediums. J Geophys Res 74:1614–1634. https://doi.org/10.1029/jb074i006p01614

Davidsson BJR, Hosseini S (2021) Implications of surface roughness in models of water desorption on the Moon. Mon Not R Astron Soc 506:3421–3429. https://doi.org/10.1093/mnras/stab1360

Davidsson BJR, Rickman H, Bandfield JL, Groussin O, Gutiérrez PJ, Wilska M, Capria MT, Emery JP, Helbert J, Jorda L, Maturilli A, Mueller TG (2015) Interpretation of thermal emission. I. The effect of roughness for spatially resolved atmosphereless bodies. Icarus 252:1–21. https://doi.org/10.1016/j.icarus.2014.12.029

Fountain JA, West EA (1970) Thermal conductivity of particulate basalt as a function of density in simulated lunar and Martian environments. J Geophys Res 75:4063–4069. https://doi.org/10.1029/jb075i020p04063

Fukuhara T, Taguchi M, Imamura T, Nakamura M, Ueno M, Suzuki M, Iwagami N, Sato M, Mitsuyama K, Hashimoto GL, Ohshima R, Kouyama T, Ando H, Futaguchi M (2011) LIR: Longwave infrared camera onboard the venus orbiter Akatsuki. Earth Planets Space 63:1009–1018. https://doi.org/10.5047/eps.2011.06.019

Greenhagen BT, Lucey PG, Wyatt MB, Glotch TD, Allen CC, Arnold JA, Bandfield JL, Bowles NE, Hanna KLD, Hayne PO, Song E, Thomas IR, Paige DA (2010) Global silicate mineralogy of the moon from the diviner lunar radiometer. Science 1979(329):1507–1509. https://doi.org/10.1126/science.1192196

Griffith PC (2015) Advanced Himawari Imager (AHI) design and operational flexibility. In: The sixth Asia oceania meteorological satellite users' conference (AOMSUC-6), November 2015, Tokyo, Japan

Grott M, Knollenberg J, Borgs B, Hänschke F, Kessler E, Helbert J, Maturilli A, Müller N (2017) The MASCOT radiometer MARA for the Hayabusa 2 mission. Space Sci Rev. https://doi.org/10.1007/s11214-016-0272-1

Hapke B (1984) Bidirectional reflectance spectroscopy. Icarus 59:41–59. https://doi.org/10.1016/0019-1035(84)90054-X

Hayne PO, Bandfield JL, Siegler MA, Vasavada AR, Ghent RR, Williams JP, Greenhagen BT, Aharonson O, Elder CM, Lucey PG, Paige DA (2017) Global regolith thermophysical properties of the moon from the diviner lunar radiometer experiment. J Geophys Res 122:2371–2400. https://doi.org/10.1002/2017JE005387

Helfenstein P, Shepard MK (1999) Submillimeter-scale topography of the lunar regolith. Icarus 141:107–131. https://doi.org/10.1006/icar.1999.6160

Hemingway BS, Krupka KM, Robie RA (1981) Heat capacities of the alkali feldspars between 350 and 1000 K from differential scanning calorimetry, the thermodynamic functions of the alkali feldspars from 298.15 to 1400 K, and the reaction quartz + jadeite = analbite. Am Miner 66:1202–1215

Hiesinger H, Helbert J, Alemanno G, Bauch KE, D'Amore M, Maturilli A, Morlok A, Reitze MP, Stangarone C, Stojic AN, Varatharajan I, Weber I, Arnold G, Banaszkiewicz M, Bauch K, Benkhoff J, Bischoff A, Blecka M, Bowles N, Calcutt S, Colangeli L, D'Amore M, Erard S, Fonti S, Greenhagen BT, Groussain O, Helbert J, Hiesinger H, Hirsch H, Jahn J, Killen R, Knollenberg J, Kührt E, Lorenz E, Mann I, Mall U, Maturilli A, Morlok A, Moroz L, Peter G, Rataj M, Robinson M, Skrbek W, Spohn T, Sprague A, Stöffler D, Stojic A, Taylor F, Varatharajan I, Venus H, Warrell J, Walter I, Weber I, Witzke A, Wöhler C (2020) Studying the composition and mineralogy of the Hermean surface with the Mercury Radiometer and Thermal Infrared Spectrometer (MERTIS) for the BepiColombo mission: an update. Space Sci Rev. https://doi.org/10.1007/s11214-020-00732-4

Honniball CI, Lucey PG, Li S, Shenoy S, Orlando TM, Hibbitts CA, Hurley DM, Farrell WM (2021) Molecular water detected on the sunlit Moon by SOFIA. Nature Astronomy 5:121–127. https://doi.org/10.1038/s41550-020-01222-x

Horai K, Simmons G (1972) Thermal property measurements on lunar material returned by Apollo 11 and 12 missions, In: Thermal characteristics of the moon. pp. 243–267. https://doi.org/10.2514/5.9781600865022.0243.0267

Howett CJA, Spencer JR, Pearl J, Segura M (2010) Thermal inertia and bolometric Bond albedo values for Mimas, Enceladus, Tethys, Dione, Rhea and Iapetus as derived from Cassini/CIRS measurements. Icarus 206:573–593. https://doi.org/10.1016/j.icarus.2009.07.016

Japan Meteorological Agency (2017) Himawari Standard Data user's guide (Version 1.3). https://www.data.jma.go.jp/mscweb/en/himawari89/space_segment/hsd_sample/HS_D_users_guide_en_v13.pdf

Keihm SJ (1984) Interpretation of the lunar microwave brightness temperature spectrum: Feasibility of orbital heat flow mapping. Icarus 60:568–589. https://doi.org/10.1016/0019-1035(84)90165-9

Keller GR, Chang T, Xiong XJ (2017) MTF analysis using lunar observations for Himawari-8/AHI. SPIE-Intl Soc Optical Eng, DOI 10(1117/12):2274091

Kiefer WS, MacKe RJ, Britt DT, Irving AJ, Consolmagno GJ (2012) The density and porosity of lunar rocks. Geophys Res Lett. https://doi.org/10.1029/2012GL051319

Kopp G, Lean JL (2011) A new, lower value of total solar irradiance: evidence and climate significance. Geophys Res Lett. https://doi.org/10.1029/2010GL045777

Kreslavsky MA, Head JW, Neumann GA, Rosenburg MA, Aharonson O, Smith DE, Zuber MT (2013) Lunar topographic roughness maps from Lunar Orbiter Laser Altimeter (LOLA) data: Scale dependence and correlation with geologic features and units. Icarus 226:52–66. https://doi.org/10.1016/j.icarus.2013.04.027

Langseth MG, Keihm SJ, Peters K (1976) Revised lunar heat-flow values. In: Lunar science conference, 7th, Houston, Tex., March 15–19, 1976, Proceedings, vol 3. (A77-34651 15-91) Pergamon Press, Inc., New York, p 3143–3171

Ledlow MJ, Zeilik M, Burns JO, Gisler GR, Zhao J-H, Baker DN (1992) Subsurface emissions from Mercury—VLA radio observations at 2 and 6 centimeters. Astrophys J 384:640. https://doi.org/10.1086/170906

Li S, Milliken RE (2017) Water on the surface of the Moon as seen by the Moon Mineralogy Mapper: distribution, abundance, and origins. Sci Adv. https://doi.org/10.1126/sciadv.1701471

Lord SD (1992) A new software tool for computing earth's atmospheric transmission of near-and far-infrared radiation. https://ntrs.nasa.gov/citations/19930010877

Lucey PG, Greenhagen B, Donaldson Hanna K, Bowles N, Flom A, Paige DA (2021) Christiansen feature map from the lunar reconnaissance orbiter diviner lunar radiometer experiment: improved corrections and derived mineralogy. J Geophys Res. https://doi.org/10.1029/2020JE006777

Melosh HJ (1989) Impact cratering : a geologic process, Oxford monographs on geology and geophysics; no. 11. Oxford University Press ; Clarendon Press, New York ; Oxford.

Müller TG, Burgdorf M, Alí-Lagoa V, Buehler SA, Prange M (2021) The Moon at thermal infrared wavelengths: a benchmark for asteroid thermal models. Astron Astrophys. https://doi.org/10.1051/0004-6361/202039946

Nash DB, Salisbury JW (1991) Infrared reflectance spectra (2.2-15 μm) of plagioclase feldspars. Geophys Res Lett 18:1151–1154. https://doi.org/10.1029/91GL01008

Nowicki SA, Christensen PR (2007) Rock abundance on Mars from the thermal emission spectrometer. J Geophys Res 112:E05007. https://doi.org/10.1029/2006JE002798

Okada T, Fukuhara T, Tanaka S, Taguchi M, Imamura T, Arai T, Senshu H, Ogawa Y, Demura H, Kitazato K, Nakamura R, Kouyama T, Sekiguchi T, Hasegawa S, Matsunaga T, Wada T, Takita J, Sakatani N, Horikawa Y, Endo K, Helbert J, Müller TG, Hagermann A (2017) Thermal infrared imaging experiments of C-type asteroid 162173 Ryugu on Hayabusa2. Space Sci Rev. https://doi.org/10.1007/s11214-016-0286-8

Okada T, Fukuhara T, Tanaka S, Taguchi M, Arai T, Senshu H, Demura H, Ogawa Y, Kouyama T, Sakatani N, Takita J, Sekiguchi T, Helbert J, Mueller TG, Hagermann A (2018) Earth and moon observations by thermal infrared imager on Hayabusa2 and the application to detectability of asteroid 162173 Ryugu. Planet Space Sci 158:46–52. https://doi.org/10.1016/j.pss.2018.05.007

Okuyama A, Takahashi M, Date K, Hosaka K, Murata H, Tabata T, Yoshino R (2018) Validation of Himawari-8/ahi radiometric calibration based on two years of in-orbit data. J Meteorol Soc Jpn 96B:91. https://doi.org/10.2151/jmsj.2018-033

Paige DA, Foote MC, Greenhagen BT, Schofield JT, Calcutt S, Vasavada AR, Preston DJ, Taylor FW, Allen CC, Snook KJ, Jakosky BM, Murray BC, Soderblom LA, Jau B, Loring S, Bulharowski J, Bowles NE, Thomas IR, Sullivan MT, Avis C, de Jong EM, Hartford W, McCleese DJ (2010) The lunar reconnaissance orbiter diviner lunar radiometer experiment. Space Sci Rev 150:125–160. https://doi.org/10.1007/s11214-009-9529-2

Pieters CM (1983) Strength of mineral absorption features in the transmitted component of near-infrared reflected light: first results from RELAB. J Geophys Res 88:9534–9544. https://doi.org/10.1029/JB088iB11p09534

Pieters CM, Goswami JN, Clark RN, Annadurai M, Boardman J, Buratti B, Combe JP, Dyar MD, Green R, Head JW, Hibbitts C, Hicks M, Isaacson P, Klima R, Kramer G, Kumar S, Livo E, Lundeen S, Malaret E, McCord T, Mustard J, Nettles J, Petro N, Runyon C, Staid M, Sunshine J, Taylor LA, Tompkins S, Varanasi P (2009) Character and spatial distribution of OH/H2O on the surface of the moon seen by M3 on chandrayaan-1. Science 1979(326):568–572. https://doi.org/10.1126/science.1178658

Rosenburg MA, Aharonson O, Head JW, Kreslavsky MA, Mazarico E, Neumann GA, Smith DE, Torrence MH, Zuber MT (2011) Global surface slopes and roughness of the Moon from the Lunar Orbiter Laser Altimeter. J Geophys Res 116:E02001. https://doi.org/10.1029/2010JE003716

Salisbury JW, Vincent RK, Logan LM, Hunt GR (1970) Infrared emissivity of lunar surface features: 2. J geophys res 75:2671–2682. https://doi.org/10.1029/jb075i014p02671

Sanin AB, Mitrofanov IG, Litvak ML, Bakhtin BN, Bodnarik JG, Boynton WV, Chin G, Evans LG, Harshman K, Fedosov F, Golovin DV, Kozyrev AS, Livengood TA, Malakhov AV, McClanahan TP, Mokrousov MI, Starr RD, Sagdeev RZ et al (2017) Hydrogen distribution in the lunar polar regions. Icarus 283:20–30. https://doi.org/10.1016/j.icarus.2016.06.002

Shepard MK, Brackett RA, Arvidson RE (1995) Self-affine (fractal) topography: surface parameterization and radar scattering. J Geophys Res. https://doi.org/10.1029/95je00664

Shimaki Y, Senshu H, Sakatani N, Okada T, Fukuhara T, Tanaka S, Taguchi M, Arai T, Demura H, Ogawa Y, Suko K, Sekiguchi T, Kouyama T, Hasegawa S, Takita J, Matsunaga T, Imamura T, Wada T, Kitazato K, Hirata N, Hirata N, Noguchi R, Sugita S, Kikuchi S, Yamaguchi T, Ogawa N, Ono G, Mimasu Y, Yoshikawa K, Takahashi T, Takei Y, Fujii A, Takeuchi H, Yamamoto Y, Yamada M, Shirai K et al (2020) Thermophysical properties of the surface of asteroid 162173 Ryugu: infrared observations and thermal inertia mapping. Icarus. https://doi.org/10.1016/j.icarus.2020.113835

Smith BG (1967) Lunar surface roughness: shadowing and thermal emission. J Geophys Res 72:4059–4067. https://doi.org/10.1029/jz072i016p04059

Sprague AL, Kozlowski RWH, Witteborn FC, Cruikshank DP, Wooden DH (1994) Mercury: evidence for anorthosite and basalt from mid-infrared (7.3-13.5 μm) spectroscopy. Icarus 109:156–167

Sunshine JM, Farnham TL, Feaga LM, Groussin O, Merlin F, Milliken RE, A'Hearn MF (2009) Temporal and spatial variability of lunar hydration as observed by the deep impact spacecraft. Science 1979(326):565–568. https://doi.org/10.1126/science.1179788

Takahashi M, Okuyama A (2017) Introduction to the global space-based intercalibration system (GSICS) and calibration/validation of the Himawari-8/AHI visible and infrared bands. Meteorol Satell Cent Tech Note 62:1–18 (**in japanese**)

Taniguchi D, Yamazaki K, Uno S (2022) The great dimming of betelgeuse seen by the Himawari-8 meteorological satellite. Nat Astron. https://doi.org/10.1038/s41550-022-01680-5

Tatsumi E, Kouyama T, Suzuki H, Yamada M, Sakatani N, Kameda S, Yokota Y, Honda R, Morota T, Moroi K, Tanabe N, Kamiyoshihara H, Ishida M, Yoshioka K, Sato H, Honda C, Hayakawa M, Kitazato K, Sawada H, Sugita S (2019) Updated inflight calibration of Hayabusa2's optical navigation camera (ONC) for scientific observations during the cruise phase. Icarus 325:153–195. https://doi.org/10.1016/j.icarus.2019.01.015

Vasavada AR, Bandfield JL, Greenhagen BT, Hayne PO, Siegler MA, Williams J-P, Paige DA (2012) Lunar equatorial surface temperatures and regolith properties from the Diviner Lunar Radiometer Experiment. J Geophys Res. https://doi.org/10.1029/2011JE003987

Williams JP, Paige DA, Greenhagen BT, Sefton-Nash E (2017) The global surface temperatures of the moon as measured by the diviner lunar radiometer experiment. Icarus 283:300–325. https://doi.org/10.1016/j.icarus.2016.08.012

Wu B, Huang J, Li Y, Wang Y, Peng J (2018) Rock abundance and crater density in the candidate Chang'E-5 landing region on the moon. J Geophys Res 123:3256–3272. https://doi.org/10.1029/2018JE005820

Zhang J, Ping J, Zeng Z, Yang Y, Li X, Wang M (2019) Surface temperature simulation of lunar dayside and its geological applications: a case in sinus iridum. Sensors 19:5545. https://doi.org/10.3390/s19245545

Publisher's Note